Oceanic Internal Gravity Waves Radiated After a Cyclonic Surface Stress Disturbance

Georg S. Voelker, Bruce R. Sutherland, Paul G. Myers and Maren Walter

MARUM - Center for Marine Environmental Sciences,
University of Bremen, Germany
voelker@uni-bremen.de, maren.walter@uni-bremen.de

Department of Earth and Atmospheric Sciences,
University of Alberta, Edmonton, Alberta, Canada
pmyers@ualberta.ca, bsuther@ualberta.ca

Abstract

Atmospheric cyclones with strong winds significantly impact the ocean circulation, regional sea surface temperature and deep water formation in the North Atlantic. Thus they are expected to play a key role in a variety of energy transport mechanisms.
The present study investigates the generation of internal gravity waves during a geostrophic adjustment process in a Boussinesq model with axisymmetric geometry. The atmospheric disturbance is set by an idealized pulse of cyclonic wind stress with a Rankine vortex structure. Strength, radius and duration of the forcing are varied. The effect upon wave generation of stratification with variable mixed layer depth is also examined.
Results indicate that internal gravity waves are generated during and after the weakening phase of the model storm. The outward radial energy flux is dominated by waves having structure close to vertical mode-1 and with frequency close to the inertial frequency. The total radiated energy corresponds to approximately 0.2% of the wind input. Deeper mixed layer conditions as well as weaker stratification reduce this fraction.

1 Introduction

The ocean circulation, regional sea surface temperature and deep water formation in the North Atlantic are significantly influenced by atmospheric cyclones with strong winds (Condron and Renfrew, 2012; Jung et al., 2014). Thus they are expected to play a key role in a variety of energy transport mechanisms. One important mechanism is the energy transfer from the storm to the deep ocean by the excitation and propagation of internal gravity waves. It has been investigated using the simple slab model (Pollard and Millard, 1970). Also general circulation models with and without parametrization for sub-grid scale storms have been applied (Condron and Renfrew, 2012; Rimac et al., 2013). Limited direct observations of energy transfer due to cyclonic storms have been made (Gill, 1984; Firing et al., 1997).
In this study we set up idealized axisymmetric simulations to investigate the energy transfer mechanisms from a circular storm by the excitation of internal gravity waves. In particular the influence of the stratification is examined.

2 Model Setup

We use a non-linear, axisymmetric and Boussinesq model to estimate the ocean response to a circular storm (Fig. 1). It is based on the simulations perfomed by McMillan and
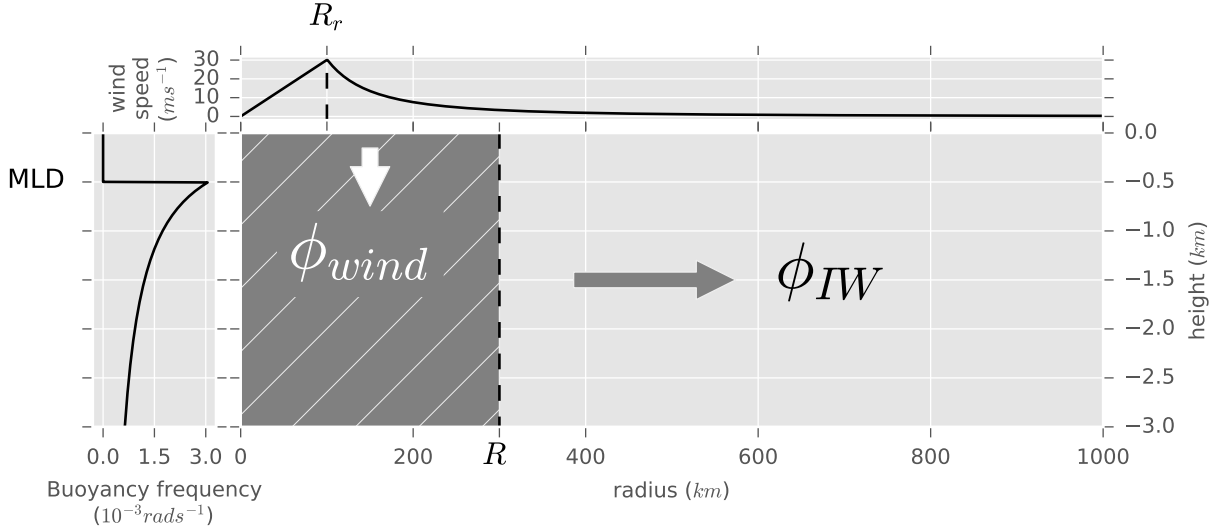
Figure 1: Schematic of the model setup. A wind cyclone with a Rankine vortex structure prescribes the surface boundary conditions (upper panel). The stratification follows Gill (1984) (left panel). The wind work ϕ_{wind} and the radiated energy flux ϕ_{IW} are estimated.

Sutherland (2010) and Holdsworth and Sutherland (2013). In particular the code solves the cylindrical Navier-Stokes equations for the pertubation density ρ, azimuthal vorticity ζ and the azimuthal velocity v. They read as follows:

$$\frac{\partial \zeta}{\partial t} = -ur\frac{\partial}{\partial r}\left(\frac{\zeta}{r}\right) - w\frac{\partial \zeta}{\partial z} + \frac{1}{r}\frac{\partial}{\partial z}\left(v^2 + fvr\right) + \frac{g}{\rho_0}\frac{\partial \rho}{\partial r} + D\left(\boldsymbol{\nu}, \zeta\right) \tag{1}$$

$$\frac{\partial v}{\partial t} = -u\frac{\partial v}{\partial r} - w\frac{\partial v}{\partial z} - \frac{1}{r}\left(uv + fur\right) + D\left(\boldsymbol{\nu}, v\right) \tag{2}$$

$$\frac{\partial \rho}{\partial t} = -u\frac{\partial \rho}{\partial r} - w\frac{\partial \rho}{\partial z} - w\frac{\partial \bar{\rho}}{\partial z} + D\left(\boldsymbol{\kappa}, \rho\right) \tag{3}$$

Here, u and w are the radial and vertical velocity respectively. f is the Coriolis frequency, g is the gravitational constant. The background and reference densities are denoted by $\bar{\rho}(z)$ and ρ_0. The dissipation operator $D(\boldsymbol{\alpha}, x)$ with a two dimensional dissipation constant $\boldsymbol{\alpha}$ and a dissipated quantity x can be written as:

$$D(\boldsymbol{\alpha}, x) = \alpha_r \frac{1}{r^2}\frac{\partial}{\partial r}\left(r^3 \frac{\partial}{\partial r}\left(\frac{x}{r}\right)\right) + \alpha_z \frac{\partial^2 x}{\partial z^2} \tag{4}$$

In our case it is used with the kinematic turbulent viscosity $\boldsymbol{\nu} = (\nu_r, \nu_z)$ for the vorticity and azimuthal velocity and the turbulent diffusivity $\boldsymbol{\kappa} = (\kappa_r, \kappa_z)$ for the density.
A stream function ψ such that $u = -\frac{\partial \psi}{\partial z}$ and $w = \frac{1}{r}\frac{\partial \psi}{\partial r}$ is derived from the vorticity using:

$$\nabla^2 \psi - \frac{\psi}{r^2} = -\zeta \tag{5}$$

with ∇^2 being the Laplacian operator in cylindrical coordinates. Eq. 5 is solved numerically with the help of the Fourier-Bessel transform in radial direction. To suppress ringing, a fourth order exponential wavenumber cutoff filter is used.
On the inner radial and bottom boundaries free-slip conditions are imposed so that normal flow is inhibited. On the surface the radial wind stress τ_r and azimuthal wind stress τ_θ are coupled to the surface velocities via the relation

Table 1: Model setup related fixed parameters.

parameter	value		comment
ν_r	1	m^2 s^{-1}	radial kinematic viscosity
ν_z	0.03	m^2 s^{-1}	vertical kinematic viscosity
ρ	1027	kg m^{-3}	reference density of sea water
ρ_{air}	1.2	kg m^{-3}	density of air
f	10^{-4}	rad s^{-1}	Coriolis frequency
Pr	1		Prandtl number
C_{10}	10^{-3}		drag coefficient
r_{max}	1000	km	maximum radius
n_r	1024		number of radial grid points
Δr	976.56	m	radial resolution
z_{min}	-3000	m	depth of domain
n_z	128		number of vertical grid points
Δz	23.44	m	vertical resolution
t_{end}	40	days	time domain
Δt	18	s	time step
n_t	20		# of steps between Euler backsteps

$$\tau_r = \nu_z \rho_0 \left(\frac{\partial u}{\partial z}\right)_{z=0} \qquad\qquad \tau_\theta = \nu_z \rho_0 \left(\frac{\partial v}{\partial z}\right)_{z=0} \qquad (6)$$

The wind stress from a wind in $10\,\mathrm{m}$ height is given by the bulk formulation

$$\boldsymbol{\tau} = \rho_{air} C_{10} \mathbf{U} |\mathbf{U}| \qquad (7)$$

$$\mathbf{U} = \begin{pmatrix} u_{10} - u|_{z=0} \\ v_{10} - v|_{z=0} \end{pmatrix} \qquad (8)$$

with the density of air ρ_{air}, the constant drag coefficient C_{10} and the velocity difference between the wind at $10\,\mathrm{m}$ height (u_{10}, v_{10}) and the surface velocity $(u|_{z=0}, v|_{z=0})$. To obtain the wind stress and the surface velocity Eq. 6 is integrated and the quadratic system is analytically solved. Note that a rigid lid condition at the surface with $w|_{z=0} = 0$ is used. Consequently the boundary condition for the azimuthal vorticity is given by $\zeta|_{z=0} = \tau_r (\nu_z \rho_0)^{-1}$. The outer radial boundary is open, approximated by a 10 point flow relaxation scheme (Jensen, 1998). Thus, internal waves do not reflect back into the domain.

The equations are discretized and solved on a staggered grid with a second-order finite-difference scheme and a leapfrog time stepping. Time splitting errors are minimized by performing an Euler backstep at regular intervals. All model related constants are summarized in Tbl. 1.

3   Initial and Surface Boundary Conditions

An ideal storm is simulated by imposing a radial profile of azimuthal wind above the surface. The Rankine vortex is chosen so that the wind has a constant vertical vorticity within a radius R_r and zero vorticity beyond. This wind structure avoids a singularity at the origin and decays beyond the critical radius R_r so that the wind is acting within a well defined domain. A pulse of wind is supplied by linearly increasing the amplitude

Table 2: Reference values for varied parameters.

parameter	value		comment
R_r	50	km	critical radius of Rankine vortex
v_r	30	m s^{-1}	maximum wind velocity at 10 m height
MLD	50	m	mixed layer depth

to its maximum in half a day, keeping it constant for one day and decreasing linearly to zero within half a day. For comparison a wind pulse with double duration of all phases is tested. The radial wind component is zero at all times.

The background density profile $\bar{\rho}(z)$ is defined so that the buoyancy frequency N corresponds to the form used by Gill (1984). In particular

$$N(z) = \begin{cases} 0, & \text{if } |z| < \text{MLD} \\ \frac{S}{z_0 - z}, & \text{if } |z| \geq \text{MLD} \end{cases} \qquad (9)$$

with $S = N_0(z_0 - z_{ref})$. Thus, the buoyancy frequency is equal to the scaling N_0 at the reference height $z_{ref} = -50$ m. The decay scaling height z_0 equals -150 m. Within the mixed layer with mixed layer depth MLD the ocean is not stratified. By varying the MLD but keeping z_{ref} constant we simulate a change of the stratification induced by variable winter cooling, impacting convection and mixed layer deepening. The reference values for varied parameters are summarized in Tbl. 2.

4 Results and Discussion

All runs reveal the same generation mechanisms of internal gravity waves. During the ramp up and the constant forcing the azimuthal velocity is accelerated. Consequently the centripetal force accelerates the water radially outward at the surface. Continuity forces upwelling at radii smaller than the critical radius of the Rankine vortex and downwelling beyond (Fig. 2a). A positive pressure anomaly at the center and a negative pressure
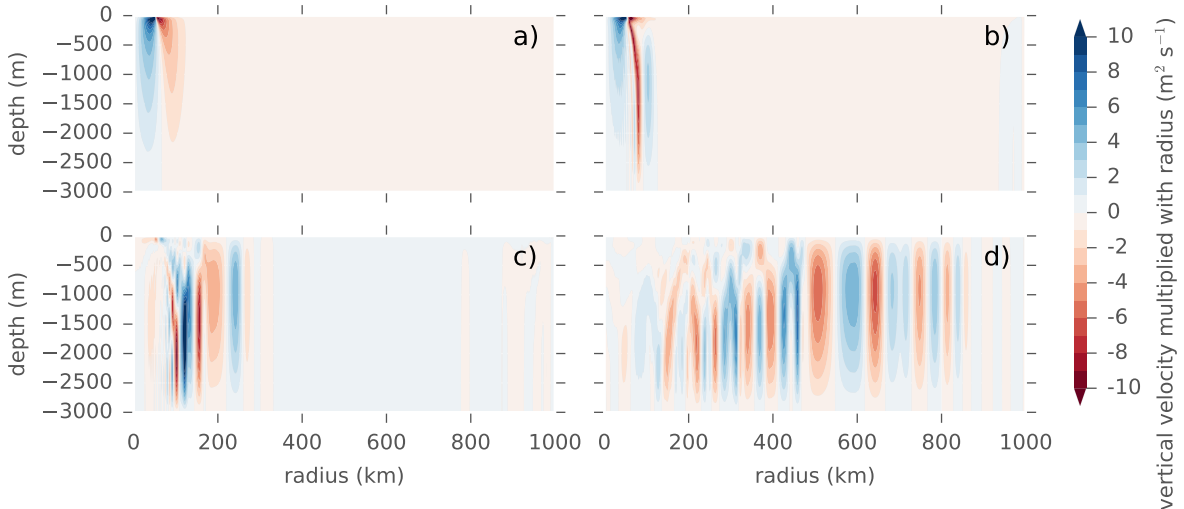

Figure 2: Snapshots of vertical velocity for the control run at model time a) 12h b) 22.5h c) 50h and d) 150h. For scaling reasons the vertical velocity was multiplied by the radius.
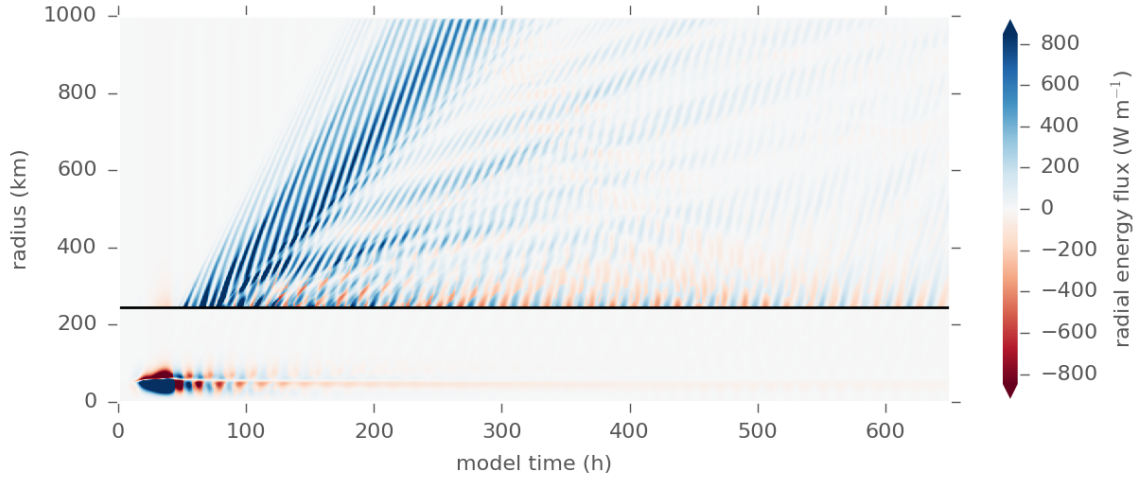
Figure 3: Largest value of the azimuthally integrated radial energy flux $2\pi R \left(u'p'\right)$ throughout the water column in the control experiment with $MLD = 50\,\mathrm{m}$. The black line marks the border between near and far field. The colorbar corresponds to the far field.

anomaly at radii larger than the critical radius develop. These pressure structures are bottom intensified. During the decrease of the wind forcing the Coriolis effect starts to counteract the described convection cell (Fig. 2b).

The inertial oscillations invert the direction of flow with the Coriolis frequency. Columnar internal gravity waves are induced through the vertical oscillation close to the critical radius (Fig. 2c).

In contrast the bottom intensified pressure structure leads to upward propagating waves with higher vertical wave number (Fig. 2d). Additionally the transition from increasing to constant wind generates a short and weak mode-1 internal gravity wave packet.
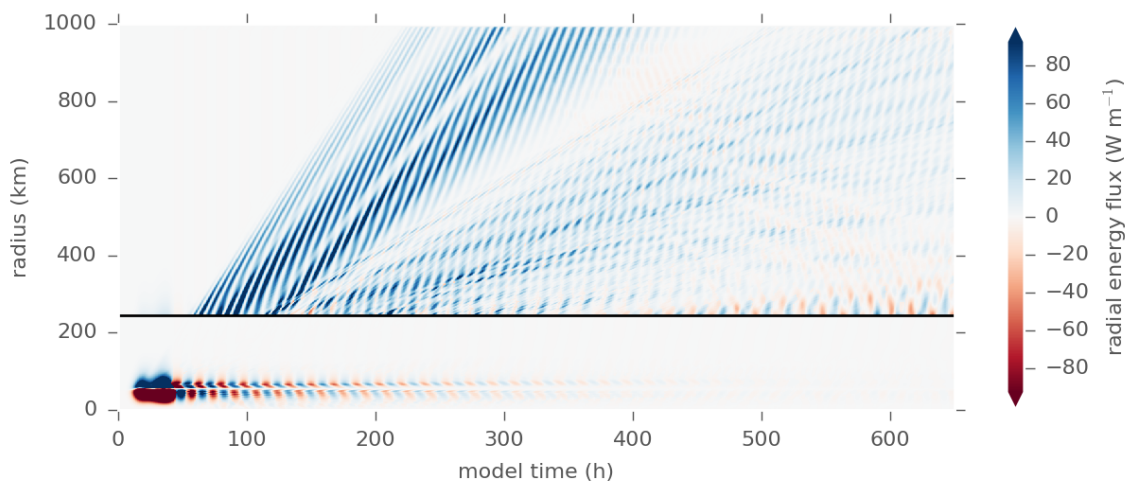

Figure 4: Largest value of the azimuthally integrated radial energy flux $2\pi R \left(u'p'\right)$ throughout the water column with $MLD = 500\,\mathrm{m}$. The black line marks the border between near and far field. The colorbar corresponds to the far field.
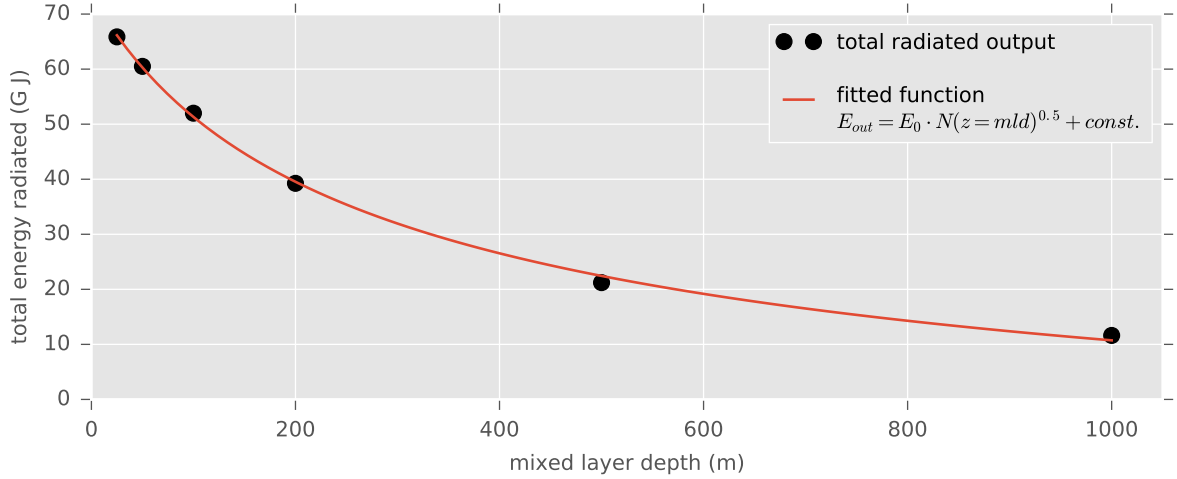
Figure 5: Total radial energy flux through a cylinder with radius $R = 500\,\text{km}$ in dependency of the buoyancy frequency at the mixed layer base $N(z = MLD)$. The red line is a fit with $E_{out} = E_0 \cdot N(z = mld)^{0.5} + const.$

The above described mechanisms are reflected in the radial energy flux through the mantle of a cylinder with radius R. Close to the critical radius the oscillation of the convection cell and the associated energy fluxes are dominant. They decay as the azimuthal velocity approaches a geostrophic equilibrium. For large enough radii, that is, in the far field the energy flux shows distinct wave packets with characteristic radial group velocities but the same frequency (Fig. 3). The differences between the group velocities originate in different vertical wave numbers. Packets with higher modes are not only generated close to the critical radius but are also radiated from lower mode packets.

To simulate the influence of mixed layer deepening. we computed a range of runs with different mixed layer depth $MLD \in \{25, 50, 100, 200, 500, 1000\}$. The structure of the wave packets radiated is generally similar to the structure of the control run. Both columnar and higher vertical mode waves are radiated from an oscillating convection cell as described above. With increasing MLD we observe a decrease of the radial group velocity as well as a decrease in energy fluxes (Fig. 4). This is because an increased mixed layer depth also means a reduced maximum in the buoyancy frequency N_{max} within the water column. We find that the energy radiated scales with $N_{max}^{0.5}$ (Fig. 5).
It is worth mentioning that the higher vertical modes are less affected by the change of the buoyancy frequency at the mixed layer base since they are generated at the bottom of the domain, where the changes in N are much smaller.

An increased critical radius leads to an increase in radial lengths scales. An increase of the radial group velocity is not observed. Higher mode waves at later times are more pronounced and show larger associated energy fluxes. We conclude that the increased critical radius leads to an increase of both radial and vertical lengths scales. The depth of the domain decreases relative to the vertical length scale and higher vertical modes become more dominant.
Structurally the simulation does not depend significantly on the wind speed. A stronger storm injects larger amounts of energy and thus the associated energy fluxes are several

orders of magnitudes larger.

5 Summary

We set up a non-linear, axisymmetric and Boussinesq model coupled to a wind at $10\,\mathrm{m}$ height. Using a pulse of wind with a Rankine vortex structure we simulated a cyclonic storm over the domain. During the descent of the wind radially propagating internal gravity waves are excited. Vertical mode-1 is dominant in the energy transfer but depends on the square root of the maximum buoyancy frequency. The energy radiated through higher vertical modes strongly depends on the lengths scales set by the wind forcing but is less sensitive to changes of the mixed layer depth.

References

Condron, A. and Renfrew, I. a. (2012). The impact of polar mesoscale storms on northeast Atlantic Ocean circulation. *Nat. Geosci.*, 6(1):34–37.

Firing, E., Lien, R.-C., and Muller, P. (1997). Observations of strong inertial oscillations after the passage of Tropical Cyclone Ofa. *J. Geophys. Res. Ocean.*, 102(C2):3317–3322.

Gill, A. E. (1984). On the Behavior of Internal Waves in the Wakes of Storms. *J. Phys. Oceanogr.*, 14(7):1129–1151.

Holdsworth, A. M. and Sutherland, B. R. (2013). Influence of lock aspect ratio upon the evolution of an axisymmetric intrusion. *J. Fluid Mech.*, 735:1–11.

Jensen, T. G. (1998). Open boundary conditions in stratified ocean models. *J. Mar. Syst.*, 16 (3-4):297–322.

Jung, T., Serrar, S., and Wang, Q. (2014). The oceanic response to mesoscale atmospheric forcing. *Geophys. Res. Lett.*, 41(4):1255–1260.

McMillan, J. M. and Sutherland, B. R. (2010). The lifecycle of axisymmetric internal solitary waves. *Nonlinear Process. Geophys.*, 2010(17):443–453.

Pollard, R. T. and Millard, R. C. (1970). Comparison between observed and simulated wind-generated inertial oscillations. *Deep. Res. Oceanogr. Abstr.*, 17(4).

Rimac, A., Von Storch, J. S., Eden, C., and Haak, H. (2013). The influence of high-resolution wind stress field on the power input to near-inertial motions in the ocean. *Geophys. Res. Lett.*, 40(18):4882–4886.